# Symmetrical Phase-Locked Loop and Power Control Loop for Grid-Connected Inverters

Yichen Sun, Xinbo Ruan, *Fellow, IEEE*, Yuying He, *Member, IEEE*, Zhiheng Lin, *Member, IEEE*, and Yiran Yan, *Student Member, IEEE*

***Abstract*—The stability of a grid-connected inverter (GCI) under weak grid can be assessed by checking whether the return ratio matrix satisfies the generalized Nyquist criterion. Due to the inherent asymmetry of the phase-locked loop (PLL) and power control loop (PCL), the eigenvalues of the return ratio matrix are complex, imposing challenges in stability analysis and parameter design of the PLL and PCL. In this article, the symmetrical PLL and PCL structures are proposed, and then a complex-vector-based model of the system is obtained, simplifying the loop-gain-based stability analysis. After that, a step-by-step parameter design method for the symmetrical PLL and PCL is presented. Experimental validation is finally conducted on a 10-kVA three-phase *LCL*-type GCI prototype in the lab. The results demonstrate the effectiveness of the proposed symmetrical PLL and PCL as well as the parameter design method.**

***Index Terms*—Grid-connected inverter (GCI), parameter design, phase-locked loop (PLL), power control loop (PCL), system stability, weak grid.**

## I. Introduction

DISTRIBUTED power generation system (DPGS) is an effective way to utilize renewable energy, such as solar and wind energy. In such system, grid-connected inverters (GCIs) act as essential energy conversion interfaces between the renewable generation units and the power grid, playing a crucial role in maintaining stable operation of DPGS [1]. With the increasing penetration of renewable energy, the power grid becomes more and more weak, and the grid impedance cannot be ignored and it varies over a wide range [2]. The interaction between GCIs and the grid impedance may lead to system instability [3], [4].

The state-space method [5], [6] and the impedance-based method [7], [8] have been widely adopted for analyzing the stability of GCI systems. The former requires formulating and solving high-order differential equations, which involves heavy computation and complex analysis. In contrast, the latter treats each device as an independent subsystem, and derives or measures its terminal impedance. The stability of the GCI system can then be assessed by applying the generalized Nyquist criterion to the return ratio matrix, defined as the product of the GCI output admittance matrix and the grid impedance matrix. However, due to the inherent asymmetry of the phase-locked loop (PLL) and power control loop (PCL), the return ratio matrix has two irrational eigenvalues, which complicates the stability analysis and parameter design [9].

As indicated in [10] and [11], when the GCI operates with a high power factor, the coupling terms in the return ratio matrix are quite smaller than the diagonal terms and can be neglected. Thus, the eigenvalues of the return ratio matrix are approximated as its diagonal elements, thereby simplifying the stability analysis. For nonunity power factor cases, the return ratio matrix is reconstructed into a singular form containing one zero eigenvalue and one nonzero eigenvalue, and the nonzero one is used to assess the system stability [12], [13]. However, the expression of the nonzero eigenvalue is still complex.

Basically, the return ratio matrix inherently represents the multiple-input multiple-output (MIMO) loop gain of the GCI system, and can be equivalently transformed into a single-input single-output (SISO) one. The equivalent SISO loop gains have been derived in the *dq*-frame [14], $\alpha\beta$-frame [15], polar-frame [16] and sequence-domain [17]. In [18], an equivalent SISO loop gain is obtained by integrating the current loop, PCL, and main circuit impedance into the PLL. Nevertheless, due to the asymmetrical PLL and PCL, the GCI output admittance matrix has coupling terms [19], resulting in complex SISO loop gains. This complexity obscures the intuitive understanding of the parameter influence on the system stability, and complicates the design of PLL and PCL parameters.

If the PLL and PCL are designed to be symmetrical, the GCI admittance matrix would become symmetrical in the *dq*-frame, with equal diagonal elements and opposite off-diagonal elements. This symmetry will enable the derivation of a complex-vector-based model which naturally exhibits the SISO characteristic [20], facilitating intuitive and straightforward stability analysis.

Recent research has paid much emphasis on achieving symmetry in PLL. In [21], [22], [23], the point of common coupling (PCC) voltage feedforward path is introduced to counteract the path introduced by the asymmetrical PLL. In [24], a symmetrical PLL is designed to yield a symmetrical transfer function matrix.

Received 13 May 2025; revised 17 August 2025 and 6 November 2025; accepted 19 December 2025. Date of publication 26 December 2025; date of current version 20 March 2026. This work was supported in part by the National Natural Science Foundation of China under Grant 52077101, in part by the Jiangsu Province 333 Program for Excellent Talents under Grant BRA2020039, and in part by the Science and Technology Project of China Southern Power Grid under Grant SEPRI-K23B081. Recommended for publication by Associate Editor B. P. McGrath. *(Corresponding author: Xinbo Ruan.)*

Yichen Sun, Xinbo Ruan, and Yiran Yan are with the Center for More-Electrical-Aircraft Power System, College of Automation Engineering, Nanjing University of Aeronautics and Astronautics, Nanjing 211106, China (e-mail: sunyichen@nuaa.edu.cn; ruanxb@nuaa.edu.cn; zjqzyyr@nuaa.edu.cn).

Yuying He is with the College of Electrical and Power Engineering, Hohai University, Nanjing 211100, China (e-mail: heyuying@hhu.edu.cn).

Zhiheng Lin is with the Department of Electrical and Computer Engineering, University of Alberta, Edmonton, AB T6G 2R3, Canada (e-mail: zhiheng.lin@ualberta.ca).

Color versions of one or more figures in this article are available at https://doi.org/10.1109/TPEL.2025.3648877.

Digital Object Identifier 10.1109/TPEL.2025.3648877

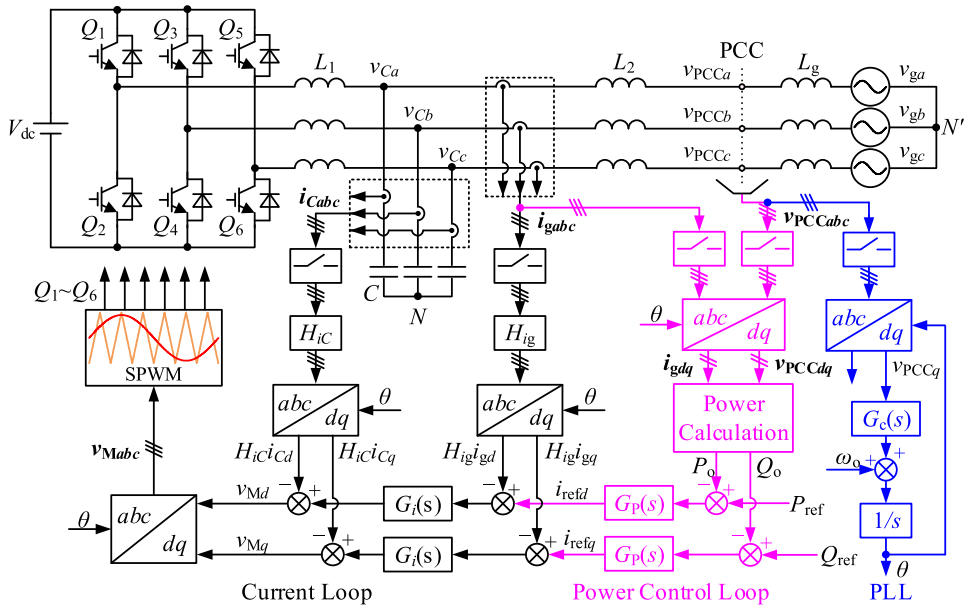


Fig. 1. Configuration of a three-phase *LCL*-type GCI.

Compared with the PCC voltage feedforward method, the symmetrical PLL does not require any additional control paths, offers simpler implementation, and has been applied in single-phase inverter systems [25], [26], three-phase inverter under unbalanced grids [27], and doubly fed induction generator systems [28]. This symmetrical PLL is deduced based on the concept of signal completeness, i.e., both the missing $d$-axis and the existing $q$-axis PCC voltage disturbances should be introduced into the Park transformation in the form of a complex vector. However, the physical mechanism of this modified transformation and a rigorous derivation for realizing model symmetry need further exploration. Additionally, the symmetrical PCL remains an ongoing research challenge.

This article presents an investigation into symmetrical PLL and PCL for simplifying stability analysis of GCI systems, and provides the parameter design method. The contributions of this article are summarized as follows.

1) The basic principles and the control structures of the symmetrical PLL and PCL are presented.
2) The mathematical model and equivalent circuit of the GCI system equipped with symmetrical PLL and PCL are established.
3) The stability-oriented parameter design method for the symmetrical PLL and PCL is provided under weak grid.

The rest of this article is organized as follows. In Section II, the mathematical models of the conventional PLL and PCL are presented. In Section III, the symmetrical PLL and PCL are proposed, and the small-signal model of the GCI with symmetrical PLL and PCL is established. In Section IV, the complex-vector-based mathematical model of the GCI system is derived, and a step-by-step parameter design method for the symmetrical PLL and PCL is given. In Section V, experiment verification on a 10-kVA three-phase *LCL*-type GCI prototype is provided. In Section VI, different stability analysis methods are compared and the benefits of the proposed symmetrical control are summarized. Finally, Section VII concludes this

## II. Modeling of Conventional PLL and PCL in GCI System

Fig. 1 shows the configuration of a three-phase *LCL*-type GCI, where $V_{\rm dc}$ is the input dc voltage, power switches $Q_1$ to $Q_6$ form the three-phase inverter bridge, inductors $L_1$ and $L_2$, and capacitor $C$ constitute the *LCL* filter, and $L_{\rm g}$ represents the grid inductance. For the convenience of illustration, the state variables in the *abc*-frame are defined as $\boldsymbol{x_{abc}} = [x_a\ x_b\ x_c]^{\rm T}$, where $x_a$, $x_b$, and $x_c$ are the $a$-, $b$-, and $c$-axis components, respectively; and the state variables in the *dq*-frame are defined as $\boldsymbol{x_{dq}} = [x_d\ x_q]^{\rm T}$, where $x_d$ and $x_q$ are the $d$- and $q$-axis components, respectively. In the control part, from right to left are the PLL, PCL, and current loop. The PLL is used to acquire the phase $\theta$ of the PCC voltage, with regulator $G_{\rm c}(s)$. The PCL generates the current reference $\boldsymbol{i_{refdq}}$ in the *dq*-frame with regulator $G_{\rm P}(s)$. The PLL and PCL regulators employ PI regulators, expressed as $G_{\rm c}(s) = k_{\rm p\_PLL} + k_{\rm i\_PLL}/s$ and $G_{\rm P}(s) = k_{\rm p\_PCL} + k_{\rm i\_PCL}/s$, respectively. The grid current $\boldsymbol{i_{g\,abc}}$ is sampled with the sense gain of $H_{ig}$, and then transformed via the Park transformation. The resultant $H_{i\,g}\boldsymbol{i_{g\,dq}}$ is compared with $\boldsymbol{i_{refdq}}$, and the error is sent to the current regulator $G_i(s)$. Capacitor current feedback with the gain of $H_{iC}$ is employed to achieve active damping of the *LCL* resonance [29]. The modulation voltage $\boldsymbol{v_{M\,dq}}$ is inversely transformed to $\boldsymbol{v_{M\,abc}}$ and then processed through the sinusoidal pulsewidth modulation to generate the driving signals for $Q_1$ to $Q_6$.

As seen from Fig. 1, the control structure of the current loop is symmetrical. The small-signal model of the Park transformation has been derived in [12], expressed as

$$\hat{\boldsymbol{x}}_{\boldsymbol{dq}} = \hat{\boldsymbol{x}}_{\boldsymbol{dq}}^{\theta_{\rm o}} + \underbrace{\frac{G_{\rm c}(s)}{s + V_{\rm PCC}dG_{\rm c}(s)}\begin{bmatrix}0 & X_q\\ 0 & -X_d\end{bmatrix}}_{\boldsymbol{G_{v\_PLL}}(s)}\hat{\boldsymbol{v}}_{\boldsymbol{PCCdq}}^{\theta_{\rm o}} \quad (1)$$

where $\theta_{\rm o}$, $X_d$, and $X_q$ are the steady-state values; $\hat{\boldsymbol{x}}_{\boldsymbol{dq}} = [\hat{x}_d,\ \hat{x}_q]^{\rm T}$ is the small-signal disturbance. The *dq* vectors with the superscript $\theta_{\rm o}$ are obtained by transforming the *abc* vectors

$$\boldsymbol{P}(\theta\ ) \qquad \hat{\boldsymbol{x}}^{\theta_{\rm o}} = \boldsymbol{P}(\theta\ )\hat{\boldsymbol{x}}_{\boldsymbol{abc}} \qquad \boldsymbol{P}(\theta\ )$$

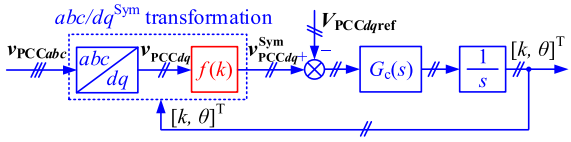


Fig. 2. General control structure of the symmetrical PLL.

as

$$\boldsymbol{P}(\theta_{\rm o})=\frac{2}{3}\begin{bmatrix}\cos\theta_{\rm o} & \cos\left(\theta_{\rm o}-\frac{2\pi}{3}\right) & \cos\left(\theta_{\rm o}+\frac{2\pi}{3}\right)\\ -\sin\theta_{\rm o} & -\sin\left(\theta_{\rm o}-\frac{2\pi}{3}\right) & -\sin\left(\theta_{\rm o}+\frac{2\pi}{3}\right)\end{bmatrix}. \tag{2}$$

The small-signal model of the power calculation is also given in [12], expressed as

$$\begin{bmatrix}\hat{P}_{\rm o}\\ \hat{Q}_{\rm o}\end{bmatrix}=\underbrace{1.5\begin{bmatrix}I_{gd} & I_{gq}\\ I_{gq} & -I_{gd}\end{bmatrix}}_{\boldsymbol{G}_{v\_\mathbf{PCL}}(s)}\hat{\boldsymbol{v}}^{\theta_{\rm o}}_{\mathbf{PCC}\boldsymbol{dq}}+\underbrace{1.5\begin{bmatrix}V_{\rm PCC}d & 0\\ 0 & V_{\rm PCC}d\end{bmatrix}}_{\boldsymbol{G}_{i\_\mathbf{PCL}}(s)}\hat{\boldsymbol{i}}^{\theta_{\rm o}}_{\mathbf{g}\boldsymbol{dq}} \tag{3}$$

where $P_{\rm o}$ and $Q_{\rm o}$ are the active and reactive power of the GCI, $V_{\rm PCC}d$, $V_{\rm PCC}q$, $I_{gd}$, and $I_{gq}$ are the steady-state values; $\hat{P}_{\rm o}$, and $\hat{Q}_{\rm o}$ are the small-signal disturbances.

As shown in (1) and (3), the PLL and PCL introduce the PCC voltage paths with asymmetrical transfer function matrices $\boldsymbol{G}_{v\_\mathbf{PLL}}(s)$ and $\boldsymbol{G}_{v\_\mathbf{PCL}}(s)$, respectively. Thus, the admittance matrix of the GCI is asymmetrical, resulting in complexity of the stability analysis and parameter design.

## III. Proposed Symmetrical PLL and PCL

### A. Proposed Symmetrical PLL

The PLL acquires the phase $\theta$ of the PCC voltage by controlling its $q$-axis component to be zero, and the dynamics of the $d$-axis component of the PCC voltage is ignored. This is the root cause of the asymmetrical small-signal model of the Park transformation shown in (1). In order to incorporate the dynamics of the $d$-axis component of the PCC voltage and avoid introducing extra rotation angle in the PCC voltage that will affect the phase acquisition, a scaling transformation $f(k)$ is added after the Park transformation, as shown in Fig. 2. This is the general control structure of the proposed symmetrical PLL. The scaling factor $k$ is the $d$-axis output. This resultant coordinate transformation is called as the $abc/dq^{\rm Sym}$ transformation. To ensure consistent dynamics between the $d$- and $q$-axis, symmetrically structured control loops are implemented for both axes.

In Fig. 2, $\boldsymbol{V}_{\mathbf{PCC}\boldsymbol{dq}\mathbf{ref}}=[V_{\rm ref},0]^{\rm T}$. Thus, the $q$-axis component of the PCC voltage after the $abc/dq^{\rm Sym}$ transformation remains zero, and the $d$-axis component is regulated at $V_{\rm ref}$. The $abc/dq^{\rm Sym}$ transformation is expressed as

$$\boldsymbol{x}^{\mathbf{Sym}}_{\boldsymbol{dq}}=f(k)\boldsymbol{P}(\theta)\boldsymbol{x}_{\boldsymbol{abc}}. \tag{4}$$

Small-signal disturbance is imposed on each variable in (4), i.e.,

$$\boldsymbol{x}^{\mathbf{Sym}}_{\boldsymbol{dq}}=\boldsymbol{X}^{\mathbf{Sym}}_{\boldsymbol{dq}}+\hat{\boldsymbol{x}}^{\mathbf{Sym}}_{\boldsymbol{dq}},\quad \boldsymbol{x}_{\boldsymbol{abc}}=\boldsymbol{X}_{\boldsymbol{abc}}+\hat{\boldsymbol{x}}_{\boldsymbol{abc}},$$
$$k=k_0+\hat{k},\quad \theta=\theta_{\rm o}+\hat{\theta} \tag{5}$$

where $\boldsymbol{X}^{\mathbf{Sym}}_{\boldsymbol{dq}}$, $\boldsymbol{X}_{\boldsymbol{abc}}$, $k_0$, and $\theta_{\rm o}$ are steady-state values, and $\hat{\boldsymbol{x}}^{\mathbf{Sym}}_{\boldsymbol{dq}}$, $\hat{\boldsymbol{x}}_{\boldsymbol{abc}}$, $\hat{k}$, and $\hat{\theta}$ are small-signal disturbances.

Substituting (5) into (4), and eliminating the steady-state values and neglecting the high-order small-signal terms, we have

$$\hat{\boldsymbol{x}}^{\mathbf{Sym}}_{\boldsymbol{dq}}=f(k_0)\hat{\boldsymbol{x}}^{\theta_{\rm o}}_{\boldsymbol{dq}}+\begin{bmatrix}f'(k_0)X_d & f(k_0)X_q\\ f'(k_0)X_q & -f(k_0)X_d\end{bmatrix}\begin{bmatrix}\hat{k}\\ \hat{\theta}\end{bmatrix} \tag{6}$$

where $\hat{\boldsymbol{x}}^{\theta_{\rm o}}_{\boldsymbol{dq}}=\boldsymbol{P}(\theta_{\rm o})\hat{\boldsymbol{x}}_{\boldsymbol{abc}}$.

As seen from (6), in order to ensure the symmetry for arbitrary variables, the following conditions must be satisfied, i.e.,

$$f'(k)=-f(k)\Rightarrow f(k)=Ce^{-k} \tag{7}$$

where $C>0$ to ensure $f(k)>0$. For simplicity, $C=1$ is chosen, which is the same as the method proposed in [24].

Based on Fig. 2, we have $[\hat{k},\ \hat{\theta}]^{\rm T}=[G_{\rm c}(s)/s]\ \hat{\boldsymbol{v}}^{\mathbf{Sym}}_{\mathbf{PCC}\boldsymbol{dq}}$. Substituting it and $f(k)=e^{-k}$ into (6), leads to

$$\hat{\boldsymbol{x}}^{\mathbf{Sym}}_{\boldsymbol{dq}}=e^{-k_0}\left(\hat{\boldsymbol{x}}^{\theta_{\rm o}}_{\boldsymbol{dq}}+\begin{bmatrix}-X_d & X_q\\ -X_q & -X_d\end{bmatrix}\frac{G_{\rm c}(s)}{s}\hat{\boldsymbol{v}}^{\mathbf{Sym}}_{\mathbf{PCC}\boldsymbol{dq}}\right) \tag{8}$$

where $e^{-k_0}=V_{\rm ref}/V_{\rm PCC}d$, which is derived considering the $d$-axis PCC voltage is scaled to $V_{\rm ref}$, and is set to 1 in [24] for simplicity.

According to (8), and keeping $V_{\rm PCC}q=0$ in mind, we have

$$\hat{\boldsymbol{v}}^{\mathbf{Sym}}_{\mathbf{PCC}\boldsymbol{dq}}=e^{-k_0}\left(\hat{\boldsymbol{v}}^{\theta_{\rm o}}_{\mathbf{PCC}\boldsymbol{dq}}-V_{\rm PCC}d\frac{G_{\rm c}(s)}{s}\hat{\boldsymbol{v}}^{\mathbf{Sym}}_{\mathbf{PCC}\boldsymbol{dq}}\right). \tag{9}$$

According to (9), we have

$$\hat{\boldsymbol{v}}^{\mathbf{Sym}}_{\mathbf{PCC}\boldsymbol{dq}}=\frac{s}{e^{k_0}s+V_{\rm PCC}dG_{\rm c}(s)}\hat{\boldsymbol{v}}^{\theta_{\rm o}}_{\mathbf{PCC}\boldsymbol{dq}}. \tag{10}$$

Substituting (10) into (8), yields

$$\hat{\boldsymbol{x}}^{\mathbf{Sym}}_{\boldsymbol{dq}}=e^{-k_0}\hat{\boldsymbol{x}}^{\theta_{\rm o}}_{\boldsymbol{dq}}+e^{-k_0}\underbrace{\frac{e^{-k_0}G_{\rm c}(s)}{s+V_{\rm ref}G_{\rm c}(s)}}_{G^{\rm Sym}_{\rm PLL}(s)}\begin{bmatrix}-X_d & X_q\\ -X_q & -X_d\end{bmatrix}\hat{\boldsymbol{v}}^{\theta_{\rm o}}_{\mathbf{PCC}\boldsymbol{dq}} \tag{11}$$

where $G^{\rm Sym}_{\rm PLL}(s)$ is the closed-loop transfer function of the symmetrical PLL.

As shown in Fig. 1, there are three coordinate transformations in the GCI. According to (11), we have

$$H_{ig}\hat{\boldsymbol{i}}^{\mathbf{Sym}}_{\mathbf{g}\boldsymbol{dq}}=e^{-k_0}H_{ig}\hat{\boldsymbol{i}}^{\theta_{\rm o}}_{\mathbf{g}\boldsymbol{dq}}+e^{-k_0}\underbrace{H_{ig}G^{\rm Sym}_{\rm PLL}(s)\begin{bmatrix}-I_{gd} & I_{gq}\\ -I_{gq} & -I_{gd}\end{bmatrix}}_{\boldsymbol{Y}^{\mathbf{Sym}}_{\mathbf{g\_PLL}}(s)}\hat{\boldsymbol{v}}^{\theta_{\rm o}}_{\mathbf{PCC}\boldsymbol{dq}} \tag{12a}$$

$$H_{iC}\hat{\boldsymbol{i}}^{\mathbf{Sym}}_{\boldsymbol{Cdq}}=e^{-k_0}H_{iC}\hat{\boldsymbol{i}}^{\theta_{\rm o}}_{\boldsymbol{Cdq}}+e^{-k_0}\underbrace{H_{iC}G^{\rm Sym}_{\rm PLL}(s)\begin{bmatrix}-I_{Cd} & I_{Cq}\\ -I_{Cq} & -I_{Cd}\end{bmatrix}}_{\boldsymbol{G}^{\mathbf{Sym}}_{\boldsymbol{iC\_PLL}}(s)}\hat{\boldsymbol{v}}^{\theta_{\rm o}}_{\mathbf{PCC}\boldsymbol{dq}} \tag{12b}$$

$$\hat{\boldsymbol{v}}^{\theta_{\rm o}}_{\mathbf{M}\boldsymbol{dq}}=e^{k_0}\hat{\boldsymbol{v}}^{\mathbf{Sym}}_{\mathbf{M}\boldsymbol{dq}}-\underbrace{G^{\rm Sym}_{\rm PLL}(s)\begin{bmatrix}-V_{\rm Md} & V_{\rm Mq}\\ -V_{\rm Mq} & -V_{\rm Md}\end{bmatrix}}_{\boldsymbol{G}^{\mathbf{Sym}}_{\mathbf{M\_PLL}}(s)}\hat{\boldsymbol{v}}^{\theta_{\rm o}}_{\mathbf{PCC}\boldsymbol{dq}} \tag{12c}$$

where $I_{Cd}$, $I_{Cq}$, $V_{\rm Md}$, and $V_{\rm Mq}$ are the steady-state values.

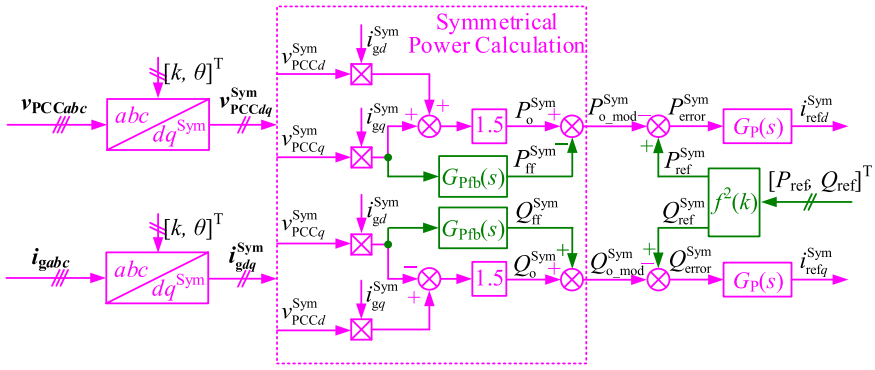


Fig. 3. Control structure of the symmetrical PCL.

As seen from (12), when adopting the symmetrical PLL, the transfer function matrices of the PCC voltage paths, $\boldsymbol{Y}^{\mathbf{Sym}}_{\mathbf{g\_PLL}}(s)$, $\boldsymbol{G}^{\mathbf{Sym}}_{\boldsymbol{iC\_PLL}}(s)$, and $\boldsymbol{G}^{\mathbf{Sym}}_{\mathbf{M\_PLL}}(s)$, are symmetrical.

Based on Fig. 2, the physical insights of the symmetrical PLL can be summarized as follows.

1) The scaling transformation $f(k)$ is used to regulate the magnitude of the PCC voltage vector to $V_{\mathrm{ref}}$.
2) The rotation transformation $abc/dq$ is employed to acquire the phase information of the PCC voltage vector.

### B. Proposed Symmetrical PCL

With the $abc/dq^{\mathrm{Sym}}$ transformation, the voltage and current vectors are scaled by a factor of $e^{-k}$, and the power is scaled by $e^{-2k}$. As a result, the original power references should be scaled by $e^{-2k}$. So, the active power and reactive power and their corresponding power references are expressed as

$$\begin{bmatrix} P^{\mathrm{Sym}}_{\mathrm{o}} \\ Q^{\mathrm{Sym}}_{\mathrm{o}} \end{bmatrix} = 1.5 \begin{bmatrix} v^{\mathrm{Sym}}_{\mathrm{PCC}d} i^{\mathrm{Sym}}_{\mathrm{g}d} + v^{\mathrm{Sym}}_{\mathrm{PCC}q} i^{\mathrm{Sym}}_{\mathrm{g}q} \\ -v^{\mathrm{Sym}}_{\mathrm{PCC}q} i^{\mathrm{Sym}}_{\mathrm{g}d} + v^{\mathrm{Sym}}_{\mathrm{PCC}d} i^{\mathrm{Sym}}_{\mathrm{g}q} \end{bmatrix} \tag{13a}$$

$$\begin{bmatrix} P^{\mathrm{Sym}}_{\mathrm{ref}} \\ Q^{\mathrm{Sym}}_{\mathrm{ref}} \end{bmatrix} = e^{-2k} \begin{bmatrix} P_{\mathrm{ref}} \\ Q_{\mathrm{ref}} \end{bmatrix}. \tag{13b}$$

Likewise, imposing small-signal disturbances into (13), and following the way given in (4), we have

$$\begin{bmatrix} \hat{P}^{\mathrm{Sym}}_{\mathrm{o}} \\ \hat{Q}^{\mathrm{Sym}}_{\mathrm{o}} \end{bmatrix} = e^{-2k_0} \left( \boldsymbol{G}_{\boldsymbol{v\_PCL}}(s) \hat{\boldsymbol{v}}^{\theta_{\mathrm{o}}}_{\mathbf{PCC}\boldsymbol{dq}} + \boldsymbol{G}_{\boldsymbol{i\_PCL}}(s) \hat{\boldsymbol{i}}^{\theta_{\mathrm{o}}}_{\boldsymbol{gdq}} - 2 \begin{bmatrix} P_{\mathrm{ref}} \\ Q_{\mathrm{ref}} \end{bmatrix} \hat{k} \right) \tag{14a}$$

$$\begin{bmatrix} \hat{P}^{\mathrm{Sym}}_{\mathrm{ref}} \\ \hat{Q}^{\mathrm{Sym}}_{\mathrm{ref}} \end{bmatrix} = e^{-2k_0} \left( \begin{bmatrix} \hat{P}_{\mathrm{ref}} \\ \hat{Q}_{\mathrm{ref}} \end{bmatrix} - 2 \begin{bmatrix} P_{\mathrm{ref}} \\ Q_{\mathrm{ref}} \end{bmatrix} \hat{k} \right). \tag{14b}$$

As seen from (3), $\boldsymbol{G}_{\boldsymbol{v\_PCL}}(s)$ is an asymmetrical matrix. To achieve symmetrical PCL, (14a) could be modified as

$$\begin{bmatrix} \hat{P}^{\mathrm{Sym}}_{\mathrm{o\_mod}} \\ \hat{Q}^{\mathrm{Sym}}_{\mathrm{o\_mod}} \end{bmatrix} = e^{-2k_0} \left( \boldsymbol{G}^{\mathbf{Sym}}_{\boldsymbol{v\_PCL}}(s) \hat{\boldsymbol{v}}^{\theta_{\mathrm{o}}}_{\mathbf{PCC}\boldsymbol{dq}} + \boldsymbol{G}_{\boldsymbol{i\_PCL}}(s) \hat{\boldsymbol{i}}^{\theta_{\mathrm{o}}}_{\boldsymbol{gdq}} - 2 \begin{bmatrix} P_{\mathrm{ref}} \\ Q_{\mathrm{ref}} \end{bmatrix} \hat{k} \right) \tag{15}$$

where $\boldsymbol{G}^{\mathbf{Sym}}_{\boldsymbol{v\_PCL}}(s)$ is a symmetrical matrix expressed as

$$\boldsymbol{G}^{\mathbf{Sym}}_{\boldsymbol{v\_PCL}}(s) = 1.5 \begin{bmatrix} I_{\mathrm{g}d} & -I_{\mathrm{g}q} \\ I_{\mathrm{g}q} & I_{\mathrm{g}d} \end{bmatrix}. \tag{16}$$

By comparing (15) with (14a), and keeping $\hat{v}^{\theta_{\mathrm{o}}}_{\mathrm{PCC}q} = (e^{k_0} + V_{\mathrm{PCC}d} G_{\mathrm{c}}(s)/s) \hat{v}^{\mathrm{Sym}}_{\mathrm{PCC}q}$ in mind according to (10), we have

$$\begin{bmatrix} \hat{P}^{\mathrm{Sym}}_{\mathrm{o\_mod}} \\ \hat{Q}^{\mathrm{Sym}}_{\mathrm{o\_mod}} \end{bmatrix} = \begin{bmatrix} \hat{P}^{\mathrm{Sym}}_{\mathrm{o}} \\ \hat{Q}^{\mathrm{Sym}}_{\mathrm{o}} \end{bmatrix} + 3 \left( 1 + V_{\mathrm{ref}} \frac{G_{\mathrm{c}}(s)}{s} \right) \begin{bmatrix} -I^{\mathrm{Sym}}_{\mathrm{g}q} \\ I^{\mathrm{Sym}}_{\mathrm{g}d} \end{bmatrix} \hat{v}^{\mathrm{Sym}}_{\mathrm{PCC}q} \tag{17}$$

where $I^{\mathrm{Sym}}_{\mathrm{g}d} = e^{-k_0} I_{\mathrm{g}d}$ and $I^{\mathrm{Sym}}_{\mathrm{g}q} = e^{-k_0} I_{\mathrm{g}q}$.

Thus, additional power feedback is introduced into the power calculation shown in (13a), and the active and reactive power calculations are modified as

$$\begin{bmatrix} P^{\mathrm{Sym}}_{\mathrm{o\_mod}} \\ Q^{\mathrm{Sym}}_{\mathrm{o\_mod}} \end{bmatrix} = \begin{bmatrix} P^{\mathrm{Sym}}_{\mathrm{o}} \\ Q^{\mathrm{Sym}}_{\mathrm{o}} \end{bmatrix} + 3 \left( 1 + V_{\mathrm{ref}} \frac{G_{\mathrm{c}}(s)}{s} \right) \begin{bmatrix} -i^{\mathrm{Sym}}_{\mathrm{g}q} \\ i^{\mathrm{Sym}}_{\mathrm{g}d} \end{bmatrix} v^{\mathrm{Sym}}_{\mathrm{PCC}q}. \tag{18}$$

According to (13b) and (18), the control structure of the symmetrical PCL is given in Fig. 3. Therein, $G_{\mathrm{Pfb}}(s) = 3(1 + V_{\mathrm{ref}} G_{\mathrm{c}}(s)/s) G_{\mathrm{HPF}}(s)$; $G_{\mathrm{HPF}}(s)$ is the high-pass filter (HPF), specifically designed to block the influence of power feedback on power calculation results at the fundamental frequency, and the corner frequency of the HPF is set to 5 Hz as recommended in [22], [30].

Based on Fig. 3, the physical insights of the symmetrical PCL are: scaling the power references by a factor of $e^{-2k}$ to counteract the influence of symmetrical PLL; and introducing power feedback terms to reconstruct the power calculation.

### C. Small-Signal Model of GCI Under Symmetrical Control

Based on Fig. 1, and according to (12), (14b), and (15), the small-signal model of three-phase *LCL*-type GCI with symmetrical control is derived, as shown in Fig. 4(a), where the digital control delay $G_{\mathrm{d}}(s)$ is modeled as $e^{-1.5sT_{\mathrm{s}}}$, including 1-period computation delay and a 0.5-period pulsewidth modulation (PWM) delay, and $T_{\mathrm{s}}$ is the sampling period [31]. The transfer function from the modulation signal $\boldsymbol{v}_{\boldsymbol{Mabc}}$ to the inverter bridge voltage $\boldsymbol{v}_{\boldsymbol{invabc}}$ is defined as $K_{\mathrm{PWM}} = V_{\mathrm{dc}}/(2V_{\mathrm{tri}})$, where $V_{\mathrm{tri}}$ is the amplitude of the triangular carrier.

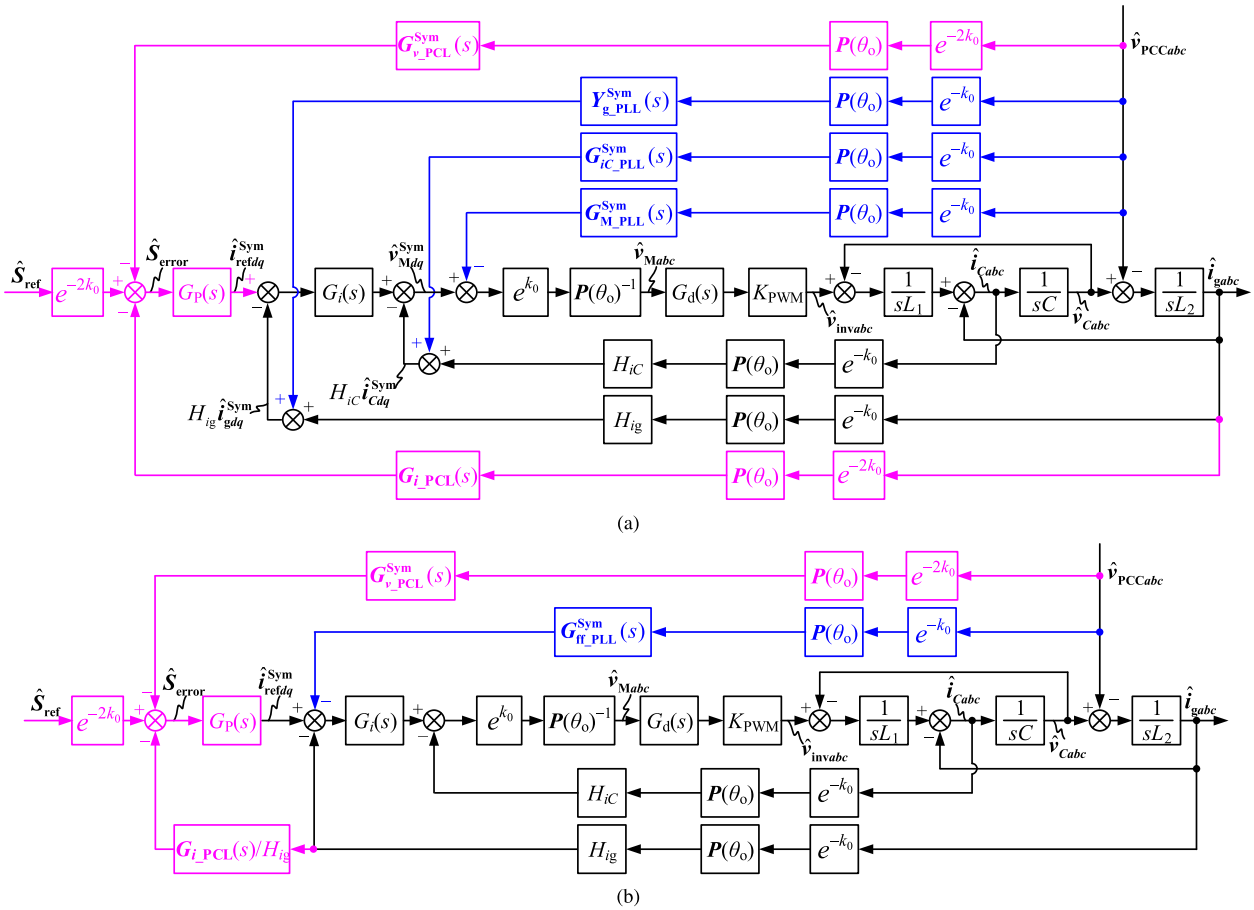


Fig. 4. Small-signal model of three-phase *LCL*-type GCI under symmetrical control. (a) Original model. (b) Equivalent model.

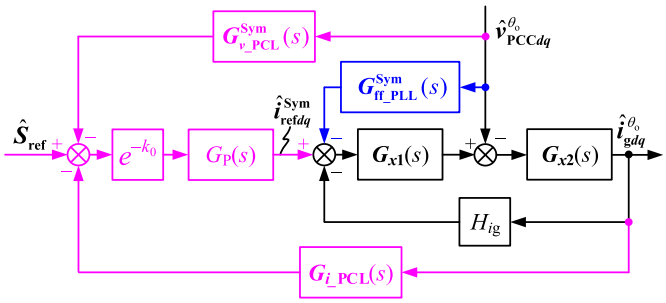

Fig. 5. Simplified small-signal model of GCI under symmetrical control.

By combining the three PCC voltage feedforward paths in Fig. 4(a) introduced by the symmetrical PLL, Fig. 4(b) is obtained, where

$$\boldsymbol{G}_{\mathbf{ff\_PLL}}^{\mathbf{Sym}}(s) = \boldsymbol{Y}_{\mathbf{g\_PLL}}^{\mathbf{Sym}}(s) + \left[\boldsymbol{G}_{\boldsymbol{iC}\mathbf{\_PLL}}^{\mathbf{Sym}}(s) + \boldsymbol{G}_{\mathbf{M\_PLL}}^{\mathbf{Sym}}(s)\right] \Big/ G_i(s). \tag{19}$$

Following the equivalent transformation method in [12], Fig. 4(b) can be further simplified to Fig. 5, where $\boldsymbol{G_{x1}}(s)$ and $\boldsymbol{G_{x2}}(s)$ are expressed as

$$\boldsymbol{G_{x1}}(s) = K_{\mathrm{PWM}} G_{\mathrm{d}}(s) G_i(s) \cdot \left[\boldsymbol{E} + \boldsymbol{Z_{L1}}(s)\boldsymbol{Z_C}^{-1}(s) + H_{iC} K_{\mathrm{PWM}} G_{\mathrm{d}}(s) \boldsymbol{Z_C}^{-1}(s)\right]^{-1}$$

$$\boldsymbol{G_{x2}}(s) = \left[\boldsymbol{E} + \boldsymbol{Z_{L1}}(s)\boldsymbol{Z_C}^{-1}(s) + H_{iC} K_{\mathrm{PWM}} G_{\mathrm{d}}(s) \boldsymbol{Z_C}^{-1}(s)\right] \cdot \begin{bmatrix} \boldsymbol{Z_{L1}}(s)\boldsymbol{Z_{L2}}(s)\boldsymbol{Z_C}^{-1}(s) + \boldsymbol{Z_{L1}}(s) + \boldsymbol{Z_{L2}}(s) \\ + H_{iC} K_{\mathrm{PWM}} G_{\mathrm{d}}(s) \boldsymbol{Z_{L2}}(s) \boldsymbol{Z_C}^{-1}(s) \end{bmatrix}^{-1} \tag{20b}$$

where $\boldsymbol{Z_{L1}}(s)$, $\boldsymbol{Z_{L2}}(s)$, and $\boldsymbol{Z_C}(s)$ are the impedance matrices of $L_1$, $L_2$, and $C$ in the $dq$-frame, respectively, expressed as [32]

$$\boldsymbol{Z_{L1}}(s) = L_1 \begin{bmatrix} s & -\omega_{\mathrm{o}} \\ \omega_{\mathrm{o}} & s \end{bmatrix}, \quad \boldsymbol{Z_{L2}}(s) = L_2 \begin{bmatrix} s & -\omega_{\mathrm{o}} \\ \omega_{\mathrm{o}} & s \end{bmatrix},$$

$$\boldsymbol{Z_C}(s) = \frac{1}{C\left(s^2 + \omega_{\mathrm{o}}^2\right)} \begin{bmatrix} s & \omega_{\mathrm{o}} \\ -\omega_{\mathrm{o}} & s \end{bmatrix}. \tag{21}$$

## IV. Parameter Design of PCL and PLL of GCI Systems Under Weak Grid

### A. Complex-Vector-Based Model of the GCI System

With the proposed symmetrical PLL and PCL, the transfer function matrices in Fig. 5 are all symmetrical matrices. When the transfer function matrix between vectors $\boldsymbol{x_{dq}}(s)$ and $\boldsymbol{y_{dq}}(s)$ in the $dq$-frame is symmetrical, i.e.,

$$\boldsymbol{y_{dq}}(s) = \begin{bmatrix} G_{dd}(s) & -G_{qd}(s) \\ G_{qd}(s) & G_{dd}(s) \end{bmatrix} \boldsymbol{x_{dq}}(s) \tag{22}$$

The complex vector $y_{dq}(s) = y_d(s) + jy_q(s)$ can be expressed as

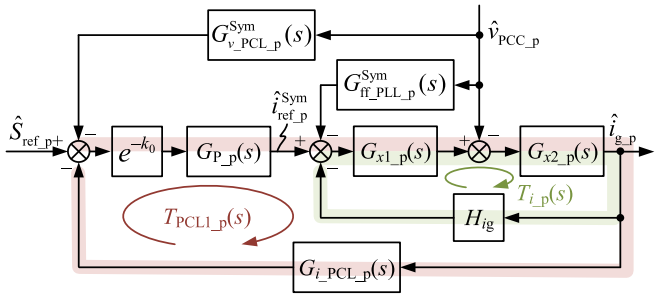


Fig. 6. The complex-vector-based model of the GCI.

i.e., the original MIMO model in the $dq$-frame can be converted to SISO model as shown in (22) and (23).

Since the rotation speeds of the complex vectors in the $dq$-frame are slower by $\omega_{\mathrm{o}}$ compared to the practical complex vectors, the latter can be obtained by a frequency shifting of $\omega_{\mathrm{o}}$, i.e., $y_{\mathrm{p}}(s) = y_{dq}(s - j\omega_{\mathrm{o}})$. So, we have

$$y_{\mathrm{p}}(s) = \left(G_{dd}(s - j\omega_{\mathrm{o}}) + jG_{qd}(s - j\omega_{\mathrm{o}})\right) x_{\mathrm{p}}(s). \tag{24}$$

By applying the transformation method from (22) to (24), (21) can be transformed into

$$Z_{L1\_\mathrm{p}}(s) = sL_1, \quad Z_{L2\_\mathrm{p}}(s) = sL_2, \quad Z_{\mathrm{C\_p}}(s) = \frac{1}{sC} \tag{25}$$

which is convenient for system modeling.

Similarly, Fig. 5 can be transformed into the complex-vector-based model, as shown in Fig. 6, where

$$G_{x1\_\mathrm{p}}(s) = \frac{K_{\mathrm{PWM}} e^{-1.5T_{\mathrm{s}}s} G_{i\_\mathrm{p}}(s)}{s^2 L_1 C + sCH_{iC}K_{\mathrm{PWM}}e^{-1.5T_{\mathrm{s}}s} + 1} \tag{26a}$$

$$G_{x2\_\mathrm{p}}(s) = \frac{s^2 L_1 C + sCH_{iC}K_{\mathrm{PWM}}e^{-1.5T_{\mathrm{s}}s} + 1}{s^3 L_1 L_2 C + s^2 CH_{iC}K_{\mathrm{PWM}}e^{-1.5T_{\mathrm{s}}s}L_2 + s\left(L_1 + L_2\right)} \tag{26b}$$

$$G^{\mathrm{Sym}}_{\mathrm{ff\_PLL\_p}}(s) = G^{\mathrm{Sym}}_{\mathrm{PLL\_p}}(s)\left[-H_{\mathrm{ig}}I_{gdq} - \left(H_{iC}I_{Cdq} + V_{\mathrm{M}dq}\right)/G_{i\_\mathrm{p}}(s)\right] \tag{26c}$$

$$\begin{aligned} G^{\mathrm{Sym}}_{v\_\mathrm{PCL\_p}}(s) &= 1.5I_{\mathrm{g}dq} \\ G_{i\_\mathrm{PCL\_p}}(s) &= 1.5V_{\mathrm{PCC}dq} \\ G_{\mathrm{P\_p}}(s) &= G_{\mathrm{P}}(s - j\omega_{\mathrm{o}}) \end{aligned} \tag{26d}$$

where $X_{dq} = X_d + jX_q$, $G_{i\_\mathrm{p}}(s) = G_i(s - j\omega_{\mathrm{o}})$, $G^{\mathrm{Sym}}_{\mathrm{PLL\_p}}(s) = G^{\mathrm{Sym}}_{\mathrm{PLL}}(s - j\omega_{\mathrm{o}})$.

The current loop gain $T_{i\_\mathrm{p}}(s)$ is expressed as

$$T_{i\_\mathrm{p}}(s) = G_{x1\_\mathrm{p}}(s)G_{x2\_\mathrm{p}}(s)H_{\mathrm{ig}} \tag{27}$$

and the PCL loop gain $T_{\mathrm{PCL1\_p}}(s)$ is expressed as

$$T_{\mathrm{PCL1\_p}}(s) = \underbrace{e^{-k_0}G_{i\_\mathrm{PCL\_p}}(s)\frac{1}{H_{\mathrm{ig}}}\frac{T_{i\_\mathrm{p}}(s)}{1 + T_{i\_\mathrm{p}}(s)}}_{T_{\mathrm{exPCL1\_p}}(s)} G_{\mathrm{P\_p}}(s). \tag{28}$$

Based on Fig. 6, the inject-grid current $\hat{i}_{\mathrm{g\_p}}(s)$ can be derived as

$$\begin{aligned} \hat{i}_{\mathrm{g\_p}}(s) = \hat{i}_{\mathrm{s\_p}}(s) - \big[&Y_{\mathrm{o\_ori\_p}}(s) + Y_{\mathrm{o\_PCL\_p}}(s) \\ &+ Y_{\mathrm{o\_PLL\_p}}(s)\big]\,\hat{v}_{\mathrm{PCC\_p}}(s) \end{aligned} \tag{29}$$

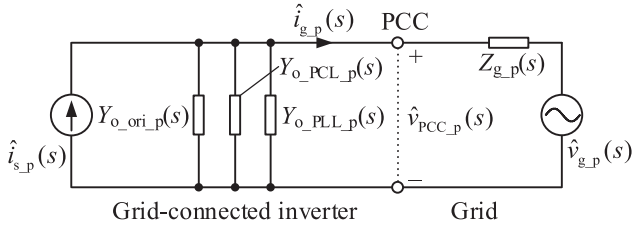


Fig. 7. Equivalent circuit of the GCI system.

where $\hat{i}_{\mathrm{s\_p}}(s)$ is the ideal current source, $Y_{\mathrm{o\_ori\_p}}(s)$ is the original admittance of the GCI, $Y_{\mathrm{o\_PLL\_p}}(s)$ is the admittance introduced by the PLL, and $Y_{\mathrm{o\_PCL\_p}}(s)$ is the admittance introduced by the PCL, which are respectively expressed as

$$\hat{i}_{\mathrm{s\_p}}(s) = \frac{T_{\mathrm{PCL1\_p}}(s)}{G_{i\_\mathrm{PCL\_p}}(s)\left(1 + T_{\mathrm{PCL1\_p}}(s)\right)}\hat{S}_{\mathrm{ref\_p}}(s) \tag{30a}$$

$$Y_{\mathrm{o\_ori\_p}}(s) = \frac{G_{x2\_\mathrm{p}}(s)}{\left(1 + T_{i\_\mathrm{p}}(s)\right)\left(1 + T_{\mathrm{PCL1\_p}}(s)\right)} \tag{30b}$$

$$Y_{\mathrm{o\_PLL\_p}}(s) = \frac{G_{x2\_\mathrm{p}}(s)G_{x1\_\mathrm{p}}(s)G^{\mathrm{Sym}}_{\mathrm{ff\_PLL\_p}}(s)}{\left(1 + T_{i\_\mathrm{p}}(s)\right)\left(1 + T_{\mathrm{PCL1\_p}}(s)\right)} \tag{30c}$$

$$Y_{\mathrm{o\_PCL\_p}}(s) = \frac{G_{x2\_\mathrm{p}}(s)G_{x1\_\mathrm{p}}(s)G_{\mathrm{P\_p}}(s)G^{\mathrm{Sym}}_{v\_\mathrm{PCL\_p}}(s)e^{-k_0}}{\left(1 + T_{i\_\mathrm{p}}(s)\right)\left(1 + T_{\mathrm{PCL1\_p}}(s)\right)}. \tag{30d}$$

Thereby, the equivalent circuit of the GCI system can be derived, as shown in Fig. 7, where the grid is modeled as an ideal voltage source $\hat{v}_{\mathrm{g\_p}}(s)$ in series with the grid impedance $Z_{\mathrm{g\_p}}(s)$, and $Z_{\mathrm{g\_p}}(s) = sL_{\mathrm{g}}$. According to Fig. 7, the system impedance ratio, which is also the minor loop gain of GCI system, is expressed as

$$T_{\mathrm{GCI\_p}}(s) = Y_{\mathrm{o\_p}}(s)Z_{\mathrm{g\_p}}(s). \tag{31}$$

For ensuring system stability, $T_{\mathrm{GCI\_p}}(s)$ should satisfy the Nyquist criterion, which requires that $1 + T_{\mathrm{GCI\_p}}(s)$ has no right half-plane (RHP) zeros. $1 + T_{\mathrm{GCI\_p}}(s)$ is expressed as

$$\begin{aligned} 1 + T_{\mathrm{GCI\_p}}(s) = &\frac{1 + T_{i\_\mathrm{p}}(s) + G_{x2\_\mathrm{p}}(s)Z_{\mathrm{g\_p}}(s)}{\left(1 + T_{i\_\mathrm{p}}(s)\right)\left(1 + T_{\mathrm{PCL1\_p}}(s)\right)} \\ &\cdot \left(1 + \underbrace{T_{\mathrm{exPCL2\_p}}(s)G_{\mathrm{P\_p}}(s)}_{T_{\mathrm{PCL2\_p}}(s)}\right) \cdot \left(1 + \underbrace{T_{\mathrm{exPLL\_p}}(s)G^{\mathrm{Sym}}_{\mathrm{PLL\_p}}(s)}_{T_{\mathrm{PLL\_p}}(s)}\right) \end{aligned} \tag{32}$$

where $T_{\mathrm{exPCL2\_p}}(s)$ and $T_{\mathrm{exPLL\_p}}(s)$ are expressed as

$$T_{\mathrm{exPCL2\_p}}(s) = \frac{T_{i\_\mathrm{p}}(s)\left(1.5V_{\mathrm{ref}} + G^{\mathrm{Sym}}_{v\_\mathrm{PCL\_p}}(s)e^{-k_0}Z_{\mathrm{g\_p}}(s)\right)}{H_{\mathrm{ig}}\left(1 + T_{i\_\mathrm{p}}(s) + G_{x2\_\mathrm{p}}(s)Z_{\mathrm{g\_p}}(s)\right)} \tag{33a}$$

$$T_{\mathrm{exPLL\_p}}(s) = \frac{Y_{\mathrm{o\_PLL\_p}}(s)Z_{\mathrm{g\_p}}(s)}{G^{\mathrm{Sym}}_{\mathrm{PLL\_p}}(s)\left[1 + \left(Y_{\mathrm{o\_ori\_p}}(s) + Y_{\mathrm{o\_PCL\_p}}(s)\right)Z_{\mathrm{g\_p}}(s)\right]}. \tag{33b}$$

With the proper design of the current loop, $(1 + T_{i\_p}(s) + G_{x2\_p}(s)\ Z_{g\_p}(s))$ in (32) do not have RHP zeros. Thus, combined with Fig. 6, the system stability can be assessed by checking whether $T_{\mathrm{PCL1\_p}}(s)$, $T_{\mathrm{PCL2\_p}}(s)$, and $T_{\mathrm{PLL\_p}}(s)$ satisfy the Nyquist criterion.

As can be observed from (28), (32), and (33), $T_{\mathrm{PCL1\_p}}(s)$, and $T_{\mathrm{PCL2\_p}}(s)$ are only related to the PCL, while $T_{\mathrm{PLL\_p}}(s)$ is related to both the PCL and PLL. So, the PCL is designed first, and then the PLL is designed.

### B. Parameter Design of PCL

When designing the PCL parameters, the Nyquist curves of $T_{\mathrm{PCL1,2\_p}}(s)$ should not circle $(-1, j0)$. Thereby, the gain margins $\mathrm{GM}_{\mathrm{PCL1,2}}$ of $T_{\mathrm{PCL1,2\_p}}(s)$ at the crossover frequencies $\omega_{\mathrm{x\_PCL1,2}}$ must exceed 0 dB, and the phase margins $\mathrm{PM}_{\mathrm{PCL1,2}}$ at the cutoff frequencies $\omega_{\mathrm{c\_PCL1,2}}$ must be greater than 0°. $\mathrm{GM}_{\mathrm{PCL1,2}}$ and $\mathrm{PM}_{\mathrm{PCL1,2}}$ are expressed as

$$\mathrm{GM}_{\mathrm{PCL1,2}} = -20\log\left|T_{\mathrm{PCL1,2\_p}}(j\omega_{\mathrm{x\_PCL1,2}})\right| \tag{34a}$$

$$\mathrm{PM}_{\mathrm{PCL1,2}} = 180^\circ + \angle T_{\mathrm{PCL1,2\_p}}(j\omega_{\mathrm{c\_PCL1,2}}) \tag{34b}$$

where $\omega_{\mathrm{x\_PCL1,2}}$ and $\omega_{\mathrm{c\_PCL1,2}}$ can be solved by

$$\angle T_{\mathrm{PCL1,2\_p}}(j\omega_{\mathrm{x\_PCL1,2}}) = 180^\circ \tag{35a}$$

$$\left|T_{\mathrm{PCL1,2\_p}}(j\omega_{\mathrm{c\_PCL1,2}})\right| = 1. \tag{35b}$$

Combining (34a) and (35a) yields the satisfactory PI parameter region of the PCL under the constraints of $\mathrm{GM}_{\mathrm{PCL1,2}}$, while combining (34b) and (35b) yields the satisfactory PI parameter region of the PCL under the constraints of $\mathrm{PM}_{\mathrm{PCL1,2}}$.

### C. Parameter Design of PLL

When designing the PLL parameters, the Nyquist curve of $T_{\mathrm{PLL\_p}}(s)$ should not circle $(-1, j0)$. Thereby, the gain margin $\mathrm{GM}_{\mathrm{PLL}}$ of $T_{\mathrm{PLL\_p}}(s)$ at the crossover frequency $\omega_{\mathrm{x\_PLL}}$ must exceed 0 dB, and the phase margin $\mathrm{PM}_{\mathrm{PLL}}$ at the cutoff frequency $\omega_{\mathrm{c\_PLL}}$ must be greater than 0°. $\mathrm{GM}_{\mathrm{PLL}}$ and $\mathrm{PM}_{\mathrm{PLL}}$ are expressed as

$$\mathrm{GM}_{\mathrm{PLL}} = -20\log\left|T_{\mathrm{PLL\_p}}(j\omega_{\mathrm{x\_PLL}})\right| \tag{36a}$$

$$\mathrm{PM}_{\mathrm{PLL}} = 180^\circ + \angle T_{\mathrm{PLL\_p}}(j\omega_{\mathrm{c\_PLL}}) \tag{36b}$$

where $\omega_{\mathrm{x\_PLL}}$ and $\omega_{\mathrm{c\_PLL}}$ can be solved by

$$\angle T_{\mathrm{PLL\_p}}(j\omega_{\mathrm{x\_PLL}}) = 180^\circ \tag{37a}$$

$$\left|T_{\mathrm{PLL\_p}}(j\omega_{\mathrm{c\_PLL}})\right| = 1. \tag{37b}$$

To mitigate the influence of background harmonics in the PCC voltage, the PLL bandwidth $f_{\mathrm{BW}}$ is typically set to be lower than one-tenth of the current loop bandwidth [33]. According to the definition of the PLL bandwidth, the magnitude of $G_{\mathrm{PLL}}^{\mathrm{Sym}}(s)$ at $f_{\mathrm{BW}}$ is 3 dB lower than its magnitude at 0 Hz, i.e.,

$$\left|G_{\mathrm{PLL}}^{\mathrm{Sym}}(j2\pi f_{\mathrm{BW}})\right| = \frac{1}{\sqrt{2}} \cdot \left|G_{\mathrm{PLL}}^{\mathrm{Sym}}(0)\right|. \tag{38}$$

Similarly, combining (36), (37), and (38), the satisfactory PI parameter region of the PLL under the constraint of $\mathrm{GM}_{\mathrm{PLL}}$, $\mathrm{PM}_{\mathrm{PLL}}$ and $f_{\mathrm{BW}}$ can be obtained.

### D. Design Procedure of PCL and PLL

Based on the above discussion, the parameter design procedure for the symmetrical PCL and PLL is outlined as follows.

TABLE I
PARAMETERS OF THE THREE-PHASE GCI

| Parameter | Symbol | Value | Parameter | Symbol | Value |
|---|---|---|---|---|---|
| Input voltage | $V_{\mathrm{dc}}$ | 700 V | Resonant frequency | $f_{\mathrm{r}}$ | 2239 Hz |
| Grid voltage | $V_{\mathrm{g}}$ | 380 V | Amplitude of the carrier | $V_{\mathrm{tri}}$ | 4.578V |
| Rated power | $S$ | 10 kVA | $K_{\mathrm{PWM}}$ | $K_{\mathrm{PWM}}$ | 76.5 |
| Fundamental frequency | $f_{\mathrm{o}}$ | 50 Hz | Grid inductor | $L_{\mathrm{g}}$ | 20.8 mH |
| Sampling frequency | $f_{\mathrm{s}}$ | 20 kHz | Proportional gain of $G_i(s)$ | $k_{\mathrm{p\_}i}$ | 1 |
| Inverter-side inductor | $L_1$ | 3200 $\mu$H | Integral gain of $G_i(s)$ | $k_{\mathrm{i\_}i}$ | 1000 |
| Filter capacitor | $C$ | 10 $\mu$F | Capacitor current sensor gain | $H_{iC}$ | 0.4 |
| Grid-side inductor | $L_2$ | 600 $\mu$H | Grid current sensor gain | $H_{ig}$ | 0.15 |

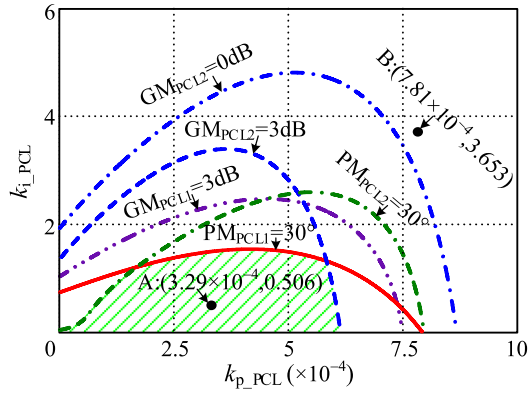


Fig. 8. Satisfactory region of PCL parameters under weak grid.

*Step 1*: Initialize $\mathrm{GM}_{\mathrm{PCL1}}$, $\mathrm{PM}_{\mathrm{PCL1}}$, $\mathrm{GM}_{\mathrm{PCL2}}$, $\mathrm{PM}_{\mathrm{PCL2}}$, $\mathrm{GM}_{\mathrm{PLL}}$, $\mathrm{PM}_{\mathrm{PLL}}$ and $f_{\mathrm{BW}}$. Normally, PM $\in$ (30°, 60°) and GM $\geq$ 3 dB are recommended for good dynamic response and robustness considering model uncertainties and parameter variations [29]. $f_{\mathrm{BW}}$ is typically set to be lower than one-tenth of the current loop bandwidth.

*Step 2*: Plot the satisfactory region of the PCL parameters under the constraints of $\mathrm{GM}_{\mathrm{PCL1}}$, $\mathrm{PM}_{\mathrm{PCL1}}$, $\mathrm{GM}_{\mathrm{PCL2}}$, and $\mathrm{PM}_{\mathrm{PCL2}}$ according to (34) and (35).

*Step 3*: Select the PCL parameters from the satisfactory region, and verify that the designed loop gains $T_{\mathrm{PCL1\_p}}(s)$ and $T_{\mathrm{PCL2\_p}}(s)$ satisfy all the afore-mentioned specifications.

*Step 4*: Plot the satisfactory region of the PLL parameters under the constraints of $\mathrm{GM}_{\mathrm{PLL}}$, $\mathrm{PM}_{\mathrm{PLL}}$, and $f_{\mathrm{BW}}$ according to (36), (37) and (38).

*Step 5*: Select the PLL parameters from the satisfactory region, and verify that the designed loop gain $T_{\mathrm{PLL\_p}}(s)$ satisfies all the aforementioned specifications.

### E. Design Example of PCL and PLL

For better understanding of the design method, a parameter design example is provided below. The key parameters of the GCI are given in Table I.

Following the above design steps 1, 2 and 3, the satisfactory region of the PCL parameters is obtained, as shown in Fig. 8. In order to verify the stability boundary of the GCI system, the

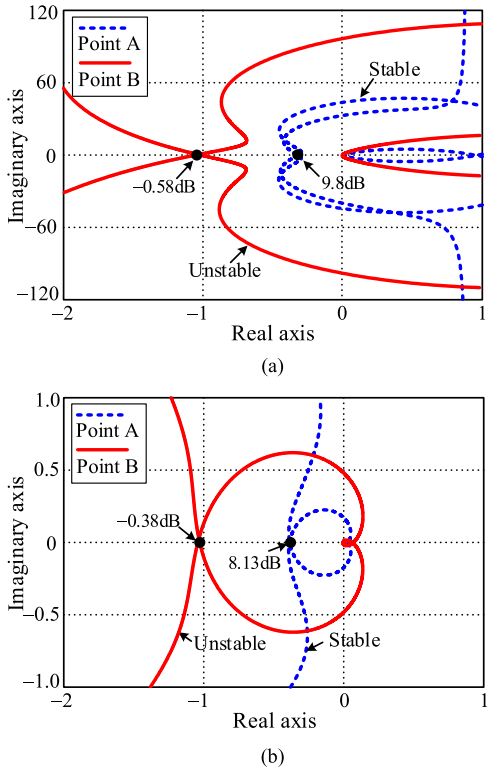


Fig. 9. Nyquist curves of $T_{\mathrm{PCL1,2\_p}}(s)$ with different PCL parameters. (a) $T_{\mathrm{PCL1\_p}}(s)$. (b) $T_{\mathrm{PCL2\_p}}(s)$.

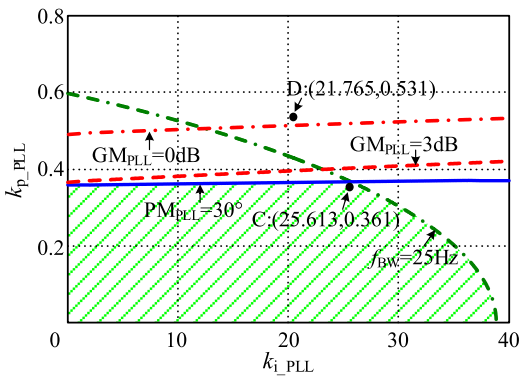


Fig. 10. Satisfactory region of PLL parameters under weak grid.

constraint of $\mathrm{GM_{PCL1}} = 0$ dB is selected to plot the unstable region of the PCL parameters. Point A ($3.29 \times 10^{-4}$, 0.506) is selected from the satisfactory region, while point B ($7.81 \times 10^{-4}$, 3.653) is selected from the unstable region for subsequent experimental comparison. Fig. 9 shows the Nyquist curves of $T_{\mathrm{PCL1\_p}}(s)$ and $T_{\mathrm{PCL2\_p}}(s)$ for points A and B. For point A, $\mathrm{GM_{PCL1}} = 9.8$ dB, $\mathrm{GM_{PCL2}} = 8.13$ dB, thus the PCL is stable, whereas for point B, $\mathrm{GM_{PCL1}} = -0.58$ dB, $\mathrm{GM_{PCL2}} = -0.38$ dB, thus the PCL is unstable.

Similarly, following the above design steps 1, 4 and 5, the satisfactory region of the PLL parameters is obtained, as shown in Fig. 10. In order to verify the stability boundary of the GCI system, the constraint of $\mathrm{GM_{PLL}} = 0$ dB is selected to plot the unstable region of the PLL parameters. Point C (25.613, 0.361) is selected from the satisfactory region, while point D (21.765, 0.531) is selected from the unstable region for comparison.

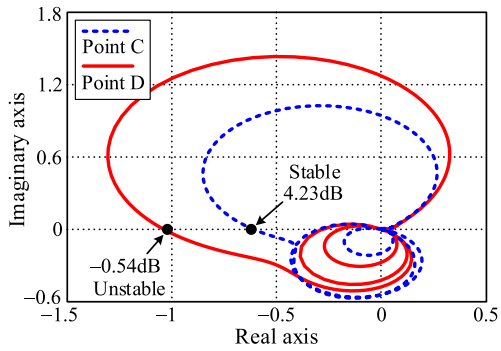


Fig. 11. Nyquist curves of $T_{\mathrm{PLL\_p}}(s)$ with different PLL parameters.

TABLE II
PARAMETERS OF THE PLL AND PCL

| Parameter | Symbol | Value | | |
|---|---|---|---|---|
| | | Set I | Set II | Set III |
| Proportional gain of $G_{\mathrm{P}}(s)$ | $k_{\mathrm{p\_PCL}}$ | $3.29 \times 10^{-4}$ | $7.81 \times 10^{-4}$ | $3.29 \times 10^{-4}$ |
| Integral gain of $G_{\mathrm{P}}(s)$ | $k_{\mathrm{i\_PCL}}$ | 0.506 | 3.653 | 0.506 |
| Proportional gain of $G_{\mathrm{c}}(s)$ | $k_{\mathrm{p\_PLL}}$ | 0.361 | 0.361 | 0.531 |
| Integral gain of $G_{\mathrm{c}}(s)$ | $k_{\mathrm{i\_PLL}}$ | 25.613 | 25.613 | 21.765 |

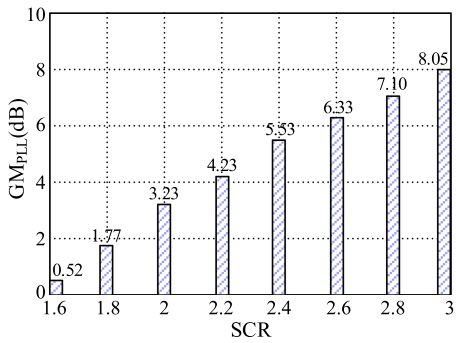


Fig. 12. Trends of $\mathrm{GM_{PLL}}$ under different SCR.

Fig. 11 shows the Nyquist curves of $T_{\mathrm{PLL\_p}}(s)$ for points C and D. For point C, $\mathrm{GM_{PLL}} = 4.23$ dB, thus the PLL is stable, whereas for point D, $\mathrm{GM_{PLL}} = -0.54$ dB, thus the PLL is unstable. Finally, the design results of the PCL and PLL parameters are shown as parameter set I in Table II. Compared with the parameters in [13], the parameters selected in this article show different stability boundaries and dynamic behaviors, which mainly results from the distinct small-signal models associated with different control methods.

As a quantitative metric of grid strength, when the short-circuit ratio (SCR) is in the range of 2 to 3, the grid is typically considered weak, and when it drops below 2, it is regarded as very weak [34]. In our laboratory setup, the SCR of the power grid with a grid inductor $L_{\mathrm{g}} = 20.8$ mH given in Table I is 2.2. Considering that the PLL is more probably to cause system instability under weak grid [9], [24], this article presents the trends of $\mathrm{GM_{PLL}}$ under different SCR, as shown in Fig. 12. As expected, $\mathrm{GM_{PLL}}$ decreases with SCR reduction. Nevertheless,

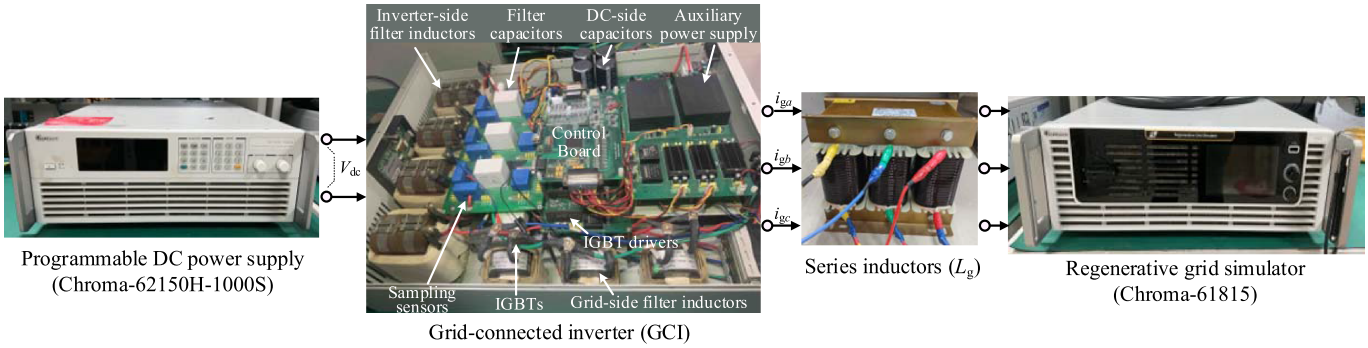


Fig. 13. Experimental setup of the three-phase *LCL*-type GCI system.

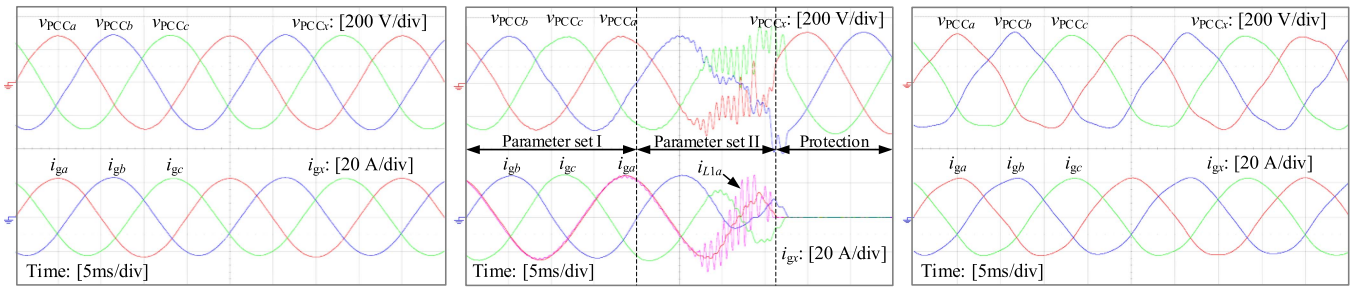


Fig. 14. Experimental waveforms of PCC voltage and current with (a) parameter set I, (b) parameter set II, and (c) parameter set III.

the designed parameters maintain acceptable stability margins in the weak grid, showing a certain degree of parameter robustness.

## V. Experimental Validation

To validate the effectiveness of the symmetrical control method and the correctness of the parameter design method, experimental verification is conducted on a 10 kVA prototype in the laboratory, with its parameters provided in Table I.

Fig. 13 shows the photograph of the experimental setup. The control scheme of the GCI is implemented through digital control on the TMS320F2812 from TI. The dc input voltage for the inverter is provided by a Chroma programmable dc power supply 62150H-1000S. The stiff grid is simulated using a Chroma regenerative grid simulator 61 815, while the grid impedance is emulated using series additional inductors.

Fig. 14 shows the experimental results of the GCI system with different parameter sets given in Table II, where parameter set I is the designed parameters, whereas parameter set II and III are the selected unstable parameters, respectively. As seen in Fig. 14(a), the PCC voltages and grid currents are sinusoidal, and the system is stable. In contrast, severe distortion appears in both the PCC voltages and grid currents in Fig. 14(b), and the system is unstable. The results validate the proposed symmetrical control method and the correctness of the PCL design results.

Similarly, as shown in Fig. 14(c), parameter set III leads to severe distortion in both PCC voltages and grid currents, which validates the proposed symmetrical control method and the correctness of the PLL parameter design method.

To exhibit the robustness of the designed parameters, Fig. 15(a) and (b) shows the experimental results of the GCI system with SCR = 2.5 and SCR = 1.9. As seen, the PCC voltages and grid currents remain stable and sinusoidal in both

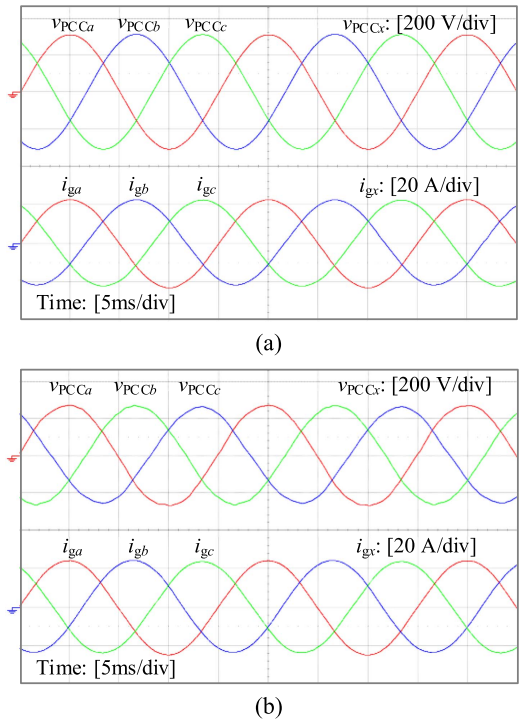


Fig. 15. Experimental waveforms of PCC voltage and current with (a) SCR = 2.5 and (b) SCR = 1.9.

cases, indicating that the designed parameters can still maintain system stability even though the grid strength changes.

Figs. 16 and 17 show the experimental results of the GCI system with sudden disturbance, e.g., single-phase and three-phase grid voltages sag to 0.9 p.u. during the fault [35],

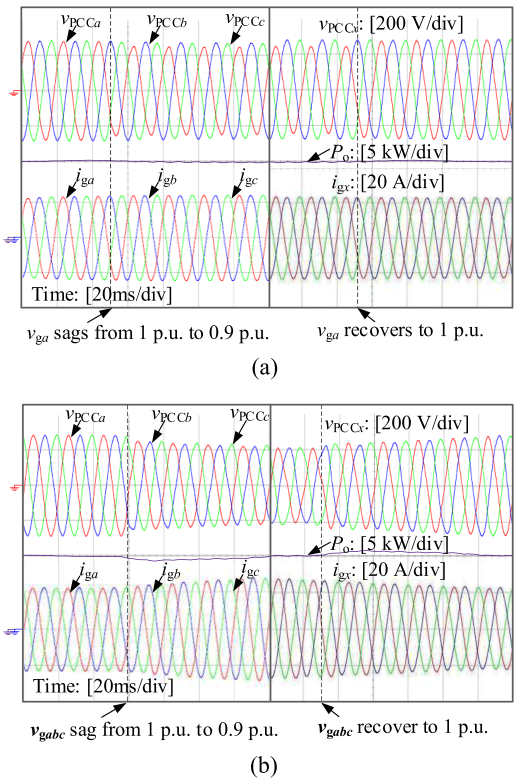


Fig. 16. Experimental waveforms of PCC voltage and current at 10 kW as (a) $v_{ga}$ sags to 0.9 p.u. and (b) $\boldsymbol{v_{gabc}}$ sag to 0.9 p.u.

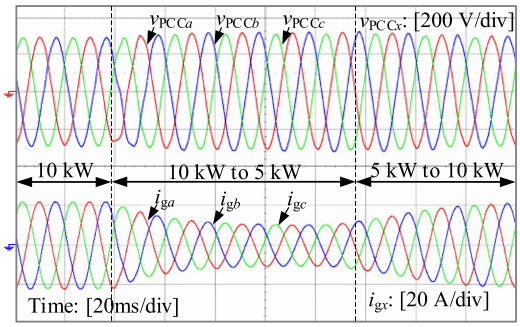


Fig. 17. Experimental waveforms of PCC voltage and current as load shifts.

and load shifts between full-load and half-load. As seen, the PCC voltages and grid currents remain stable and sinusoidal in all cases and reach new steady-state point after disturbance.

## VI. Comparison and Discussion

Table III gives the comparison between the proposed symmetrical control method with existing stability analysis methods.

The application of *D/Q* channel impedance ratio, which neglects the *dq*-frame coupling terms of the return ratio matrix, can bring the conservatism [10], [11]. Equivalent SISO loop gains in the *dq*-frame, $\alpha\beta$-frame, polar-frame and sequence domain require full consideration of coupling terms, complicating their application to simplified stability analysis [14], [15], [16], [17]. Similarly, the methods based on the reconstructed return ratio matrix and the equivalent synchronous loop gain [12], [13], [18] result in a complex non-zero eigenvalue or equivalent loop gain, due to the coupling terms in the GCI output admittance matrix.

TABLE III
Comparison of Different Stability Analysis Methods

| Stability analysis method | Model | Easy and clear for loop design? | Clear stability margin? |
|---|---|---|---|
| Return ratio matrix [9] | MIMO | No | No |
| *D/Q* channel impedance ratio [10], [11] | SISO | No | Yes |
| Reconstructed return ratio matrix [12], [13] | MIMO | Yes | Yes |
| Equivalent *dq*-frame SISO loop gain [14] | SISO | No | Yes |
| Equivalent $\alpha\beta$-frame SISO loop gain [15] | SISO | No | Yes |
| Equivalent polar-frame SISO loop gain [16] | SISO | No | Yes |
| Equivalent sequence domain SISO loop gain [17] | SISO | No | Yes |
| Equivalent synchronous loop gain [18] | SISO | Yes | Yes |
| Symmetrical control (i.e., Sym. PLL and PCL) | SISO | Yes | Yes |

In summary, due to the coupling terms in the GCI output admittance matrix, the existing stability analysis methods can hardly achieve both the simplicity and accuracy of stability analysis [9]–[18]. In contrast, with the symmetrical control structures, such as the proposed symmetrical PLL and PCL, the model can be significantly simplified, and the system impedance ratio, as expressed in (31), can be effectively used to streamline both stability analysis and parameter design.

## VII. Conclusion

Asymmetrical *dq*-frame control of the PLL and PCL yields irrational eigenvalues in the return ratio matrix, complicating the stability analysis and parameter design. In this article, the symmetrical PLL and PCL structures are proposed, and the GCI system is mathematically modeled as a complex-vector-based model. Via analyzing the minor loop gain of the GCI system, a step-by-step parameter design method for the symmetrical PLL and PCL under weak grid conditions is presented, offering both simplicity and accuracy. Finally, experimental results from a 10-kVA prototype validate the effectiveness of the proposed symmetrical control and the parameter design method.

## References

[1] Z. Lin, R. Liu, and Y. R. Li, "Transient stability analysis and coordinated phase control method for multiparallel PLL-synchronized inverters during grid fault," *IEEE Trans. Power Electron.*, vol. 40, no. 8, pp. 11442–11451, Aug. 2025.
[2] A. Etxegarai, P. Eguia, E. Torres, and E. Fernandez, "Impact of wind power in isolated power systems," in *Proc. IEEE Mediterranean Electrotech. Conf.*, 2012, pp. 63–66.
[3] N. Bottrell, M. Prodanovic, and T. C. Green, "Dynamic stability of a microgrid with an active load," *IEEE Trans. Power Electron.*, vol. 28, no. 11, pp. 5107–5119, Nov. 2013.
[4] L. P. Kunjumuhammed, B. C. Pal, C. Oates, and K. J. Dyke, "Electrical oscillations in wind farm systems: Analysis and insight based on detailed modeling," *IEEE Trans. Sustain. Energy*, vol. 7, no. 1, pp. 51–62, Jan. 2016.
[5] J. Sun, "Small-signal methods for ac distributed power systems–A review," *IEEE Trans. Power Electron.*, vol. 24, no. 11, pp. 2545–2554, Nov. 2009.
[6] L. Fan and Z. Miao, "Admittance-based stability analysis: Bode plots, Nyquist diagrams or eigenvalue analysis?" *IEEE Trans. Power Syst.*, vol. 35, no. 4, pp. 3312–3315, Jul. 2020.
[7] M. Amin and M. Molinas, "Small-signal stability assessment of power electronics based power systems: A discussion of impedance- and eigenvalue-based methods," *IEEE Trans. Ind. Appl.*, vol. 53, no. 5, pp. 5014–5030, Sep./Oct. 2017.

[8] X. Wang and F. Blaabjerg, "Harmonic stability in power electronic-based power systems: Concept, modeling, and analysis," *IEEE Trans. Smart Grid*, vol. 10, no. 3, pp. 2858–2870, May 2019.
[9] B. Wen, D. Boroyevich, R. Burgos, P. Mattavelli, and Z. Shen, "Analysis of *d-q* small-signal impedance of grid-tied inverters," *IEEE Trans. Power Electron.*, vol. 31, no. 1, pp. 675–687, Jan. 2016.
[10] B. Wen, D. Dong, D. Boroyevich, R. Burgos, P. Mattavelli, and Z. Shen, "Impedance-based analysis of grid-synchronization stability for three-phase paralleled converters," *IEEE Trans. Power Electron.*, vol. 31, no. 1, pp. 26–38, Jan. 2016.
[11] J. Yu, X. Lin, D. Song, R. Yu, J. Yang, and M. Su, "New perspectives on stability analysis of three-phase grid-connected inverter considering system couplings," *IEEE Trans. Power Syst.*, vol. 35, no. 3, pp. 1967–1978, May 2020.
[12] Y. Chen, X. Ruan, Z. Lin, Y. Yan, and Y. He, "A reconstructed singular return ratio matrix for optimizing design of the PLL in grid-connected inverters," *IEEE Trans. Ind. Electron.*, vol. 70, no. 12, pp. 12453–12464, Dec. 2023.
[13] Y. Chen, X. Ruan, Y. He, and Y. Yan, "Return ratio matrix reconstruction approach for grid-connected inverters: Principle, physical insights, and parameter design," *IEEE Trans. Power Electron.*, vol. 40, no. 4, pp. 6084–6096, Apr. 2025.
[14] H. Zhang, X. Wang, L. Harnefors, H. Gong, J.-P. Hasler, and H.-P. Nee, "SISO transfer functions for stability analysis of grid-connected voltage-source converters," *IEEE Trans. Ind. Appl.*, vol. 55, no. 3, pp. 2931–2941, May/Jun. 2019.
[15] J. Lin, M. Su, Y. Sun, S. Xie, W. Xiong, and X. Li, "Unified SISO loop gain modeling, measurement, and stability analysis of three-phase voltage source converters," *IEEE Trans. Energy Conv.*, vol. 37, no. 3, pp. 1907−1920, Sep. 2022.
[16] S. Li, Y. Yan, and X. Yuan, "SISO equivalent of MIMO VSC-dominated power systems for voltage amplitude and phase dynamic analyses in current control timescale," *IEEE Trans. Energy Conv.*, vol. 34, no. 3, pp. 1454−1465, Sep. 2019.
[17] C. Zhang, X. Cai, A. Rygg, and M. Molinas, "Sequence domain SISO equivalent models of a grid-tied voltage source converter system for small-signal stability analysis," *IEEE Trans. Energy Conv.*, vol. 33, no. 2, pp. 741−749, Jun. 2018.
[18] L. Huang et al., "Grid-synchronization stability analysis and loop shaping for PLL-based power converters with different reactive power control," *IEEE Trans. Smart Grid*, vol. 11, no. 1, pp. 501−516, Jan. 2020.
[19] S. Shah and L. Parsa, "Impedance modeling of three-phase voltage source converters in *dq*, sequence, and phasor domains," *IEEE Trans. Energy Conv.*, vol. 32, no. 3, pp. 1139−1150, Sep. 2017.
[20] A. Rygg, M. Molinas, C. Zhang, and X. Cai, "On the equivalence and impact on stability of impedance modeling of power electronic converters in different domains," *IEEE J. Emerg. Sel. Topics Power Electron.*, vol. 5, no. 4, pp. 1444−1454, Dec. 2017.
[21] X. Zhang, D. Xia, Z. Fu, G. Wang, and D. Xu, "An improved feedforward control method considering PLL dynamics to improve weak grid stability of grid-connected inverters," *IEEE Trans. Ind. Appl.*, vol. 54, no. 5, pp. 5143−5151, Sep./Oct. 2018.
[22] X. Zhang, S. Fu, W. Chen, N. Zhao, G. Wang, and D. Xu, "A symmetrical control method for grid-connected converters to suppress the frequency coupling under weak grid conditions," *IEEE Trans. Power Electron.*, vol. 35, no. 12, pp. 13488−13499, Dec. 2020.
[23] X. Tang, Z. Li, W. Wang, L. Liu, B. Qu, and J. M. Guerrero, "A decoupling control method for converting DIDO sequence admittance model of grid-tied converter system into SISO," *IEEE Trans. Energy Conv.*, vol. 38, no. 4, pp. 2647−2661, Dec. 2023.
[24] D. Yang, X. Wang, F. Liu, K. Xin, Y. Liu, and F. Blaabjerg, "Symmetrical PLL for SISO impedance modeling and enhanced stability in weak grids," *IEEE Trans. Power Electron.*, vol. 35, no. 2, pp. 1473−1483, Feb. 2020.
[25] J. Lin et al., "Frequency coupling suppression control strategy for single-phase grid-tied inverters in weak grid," *IEEE Trans. Ind. Electron.*, vol. 69, no. 9, pp. 8926−8938, Sep. 2022.
[26] Z. Lin et al., "Asymmetric synchronous reference frame-based frequency coupling suppression control for single-phase grid-tied converters," *IEEE Trans. Ind. Electron.*, vol. 71, no. 12, pp. 15704−15713, Dec. 2024.
[27] H. Li, Y. Sun, J. Lin, X. Li, Y. Liu, and M. Su, "Inductance-emulating-based frequency coupling suppression control for three-phase grid-tied VSC under unbalanced grids," *IEEE Trans. Power Electron.*, vol. 39, no. 10, pp. 12371−12383, Oct. 2024.
[28] B. Hu, H. Nian, M. Li, Y. Xu, Y. Liao, and J. Yang, "Impedance-based analysis and stability improvement of DFIG system within PLL bandwidth," *IEEE Trans. Ind. Electron.*, vol. 69, no. 6, pp. 5803−5814, Jun. 2022.
[29] X. Wang, C. Bao, X. Ruan, W. Li, and D. Pan, "Design considerations of digitally controlled *LCL*-filtered inverter with capacitor-current-feedback active damping," *IEEE J. Emerg. Sel. Topics Power Electron.*, vol. 2, no. 4, pp. 972−984, Dec. 2014.
[30] X. Xiong, B. Luo, L. Li, Z. Sun, and F. Blaabjerg, "Impedance reshaping method of DFIG system based on compensating rotor current dynamic to eliminate PLL influence," *IEEE Trans. Power Electron.*, vol. 39, no. 4, pp. 4006−4016, Apr. 2024.
[31] D. Yang, X. Ruan, and H. Wu, "A real-time computation method with dual sampling mode to improve the current control performance of the *LCL*-type grid-connected inverter," *IEEE Trans. Ind. Electron.*, vol. 62, no. 7, pp. 4563−4572, Jul. 2015.
[32] X. Wang, L. Harnefors, and F. Blaabjerg, "Unified impedance model of grid-connected voltage-source converters," *IEEE Trans. Power Electro.*, vol. 33, no. 2, pp. 1775−1787, Feb. 2018.
[33] L. Harnefors, M. Bongiorno, and S. Lundberg, "Input-admittance calculation and shaping for controlled voltage-source converters," *IEEE Trans. Ind. Electron.*, vol. 54, no. 6, pp. 3323−3334, Dec. 2007.
[34] A. A. A. Radwan and Y. A.-R. I. Mohamed, "Improved vector control strategy for current-source converters connected to very weak grids," *IEEE Trans. Power Syst.*, vol. 31, no. 4, pp. 3238−3248, Jul. 2016.
[35] P. Ge, C. Tu, F. Xiao, Q. Guo, and J. Gao, "Design-oriented analysis and transient stability enhancement control for a virtual synchronous generator," *IEEE Trans. Ind. Electron.*, vol. 70, no. 3, pp. 2675−2684, Mar. 2023.

**Yichen Sun** received the B.S. degree in electrical engineering and automation in 2023 from Nanjing University of Aeronautics and Astronautics, Nanjing, China, where he is currently working toward the M.S. degree in electrical engineering.

His current research interests include renewable energy generation system and stability analysis of grid-connected inverter system.

**Xinbo Ruan** (Fellow, IEEE) received the B.S. and Ph.D. degrees in electrical engineering from Nanjing University of Aeronautics and Astronautics (NUAA), Nanjing, China, in 1991 and 1996, respectively.

In 1996, he was with the Faculty of Electrical Engineering Teaching and Research Division, NUAA, where he became a Professor with the College of Automation Engineering in 2002. From August to October 2007, he was a Research Fellow with the Department of Electronic and Information Engineering, Hong Kong Polytechnic University, Hong Kong. From March 2008 to August 2011, he was also with the School of Electrical and Electronic Engineering, Huazhong University of Science and Technology, Wuhan, China. He has authored or coauthored 15 books and more than 300 technical papers published in journals and conferences. His main research interests include resonant and soft-switching power converters, power converter topologies and control, grid-connected converters and system for renewable energy, modeling and stability of power converters, and envelop tracking power supply.

Dr. Ruan is currently an Editor for IEEE JOURNAL ON EMERGING AND SELECTED TOPICS ON POWER ELECTRONICS, a Co-Editor-in-Chief for IEEE TRANSACTIONS ON POWER ELECTRONICS, and an Associate Editor for IEEE OPEN JOURNAL OF THE INDUSTRIAL ELECTRONICS SOCIETY, IEEE TRANSACTIONS ON INDUSTRIAL ELECTRONICS (2011–2021), and IEEE TRANSACTIONS ON CIRCUITS AND SYSTEMS - II: EXPRESS BRIEFS (2016–2023). He was the General Chair of IPEMC-ECCE Asia 2020 and the General Secretary of IPEMC-ECCE Asia 2009, a Technical Program Committee Chair of the IEEE 7th Annual Energy Conversion Congress and Exposition, and a Tutorial Committee Chair of the IEEE 12th Annual Energy Conversion Congress and Exposition. From 2005 to 2013, and since 2017 again, he has been a Vice President of the China Power Supply Society. From 2014 to 2016, he was the Vice Chair of the Technical Committee on Renewable Energy Systems within the IEEE Industrial Electronics Society. He was the recipient of the Sustainable Energy Systems Technical Achievement Award from IEEE Power Electronics Society in 2022, the Delta Scholarship by the Delta Environment and Education Fund in 2003, and the Special Appointed Professor of the Chang Jiang Scholars Program by the Ministry of Education, China, in 2007.

**Yuying He** (Member, IEEE) received the B.S. degree from Central South University, Changsha, China, in 2015, and the Ph. D. degree from Huazhong University of Science and Technology, Wuhan, China, in 2022, both in electrical engineering.

From 2021 to 2022, she was also with E. ON Energy Research Center, RWTH Aachen University, Aachen, Germany. Since June 2022, she has been a tenure-track Associate Professor with Hohai University, Nanjing, China. Her research interests include modeling and control of grid-connected converters, harmonics analysis and control, and stability of renewable energy generation system.

**Zhiheng Lin** (Member, IEEE) received the B.S. and Ph.D. degrees in electrical engineering from Nanjing University of Aeronautics and Astronautics, Nanjing, China, in 2017 and 2022, respectively.

Since 2023, he has been a Postdoctoral Fellow with the University of Alberta, Edmonton, AB, USA. His current research interests include renewable energy generation systems, stability analysis of grid-connected inverter systems and microgrid control techniques.

Dr. Lin is the current Vice Chair of IEEE Power Electronics Society (PELS) Students and Young Professionals (S&YP) Committee. He was the Vice Chair of IEEE PELS Membership Committee—China on YP from 2022 to 2023. He was the General Co-Chair of 2023 IEEE PELS Student and Young Professionals Symposium (SYPS).

**Yiran Yan** (Student Member, IEEE) received the B.S. degree in electrical engineering from Jiangnan University, Wuxi, China, in 2017, and the M.S. degree in power electronics and power drives from Nanjing University of Science and Technology, Nanjing, China, in 2020. He is currently working toward the Ph.D. degree in electrical engineering with Nanjing University of Aeronautics and Astronautics, Nanjing, China.

His current research interests include digital control technique and renewable energy generation system.